Supporting Information

Self-templating Scheme for the Synthesis of $NiCo_2Se_4$ and BiSe Hollow Microspheres for High-energy Density Asymmetric Supercapacitors

Jingjing Xia,[a] Liuming Zhang,[a] Shouguo Xuan,[a] Yonghong Ni*,[a] Li Zhang*[ab]

[a]The Key Laboratory of Functional Molecular Solids, Ministry of Education, Key Laboratory of Electrochemical Clean Energy of Anhui Higher Education Institutes, College of Chemistry and Materials Science, Anhui Normal University, Wuhu 241000, P. R. China

[b]School of Pharmacy, Shanghai University of Medicine and Health Sciences, Shanghai 201318, P. R. China

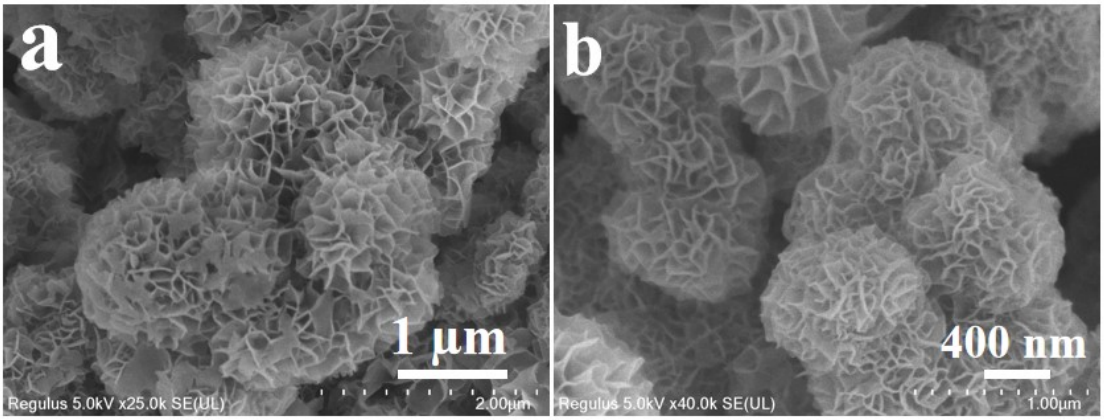

Figure S1. (a, b) SEM images of Ni-Co-LDH/C precursor.

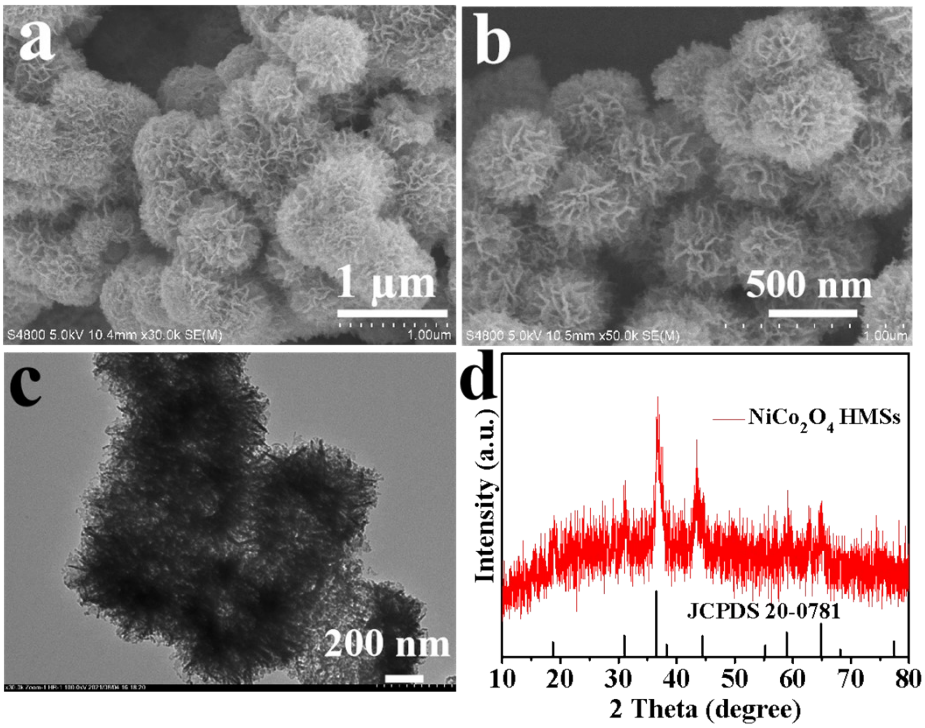

Figure S2. (a, b) SEM images, (c) TEM image and (d) XRD pattern of $NiCo_2O_4$ HMSs.

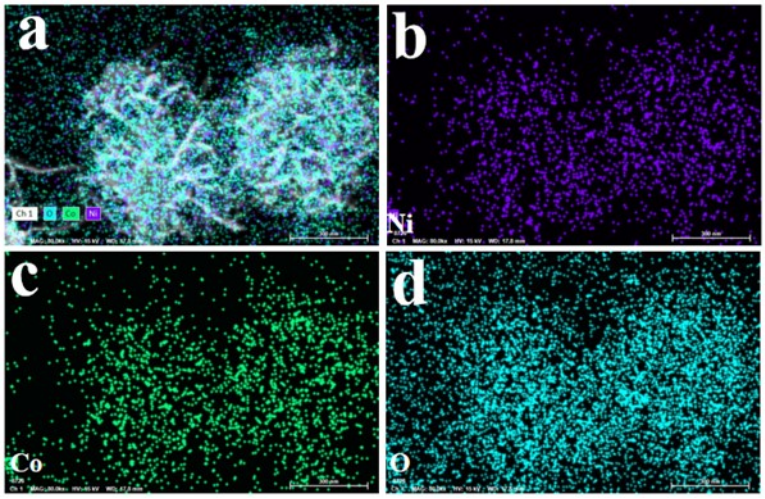

Figure S3. The SEM mapping images of $NiCo_2O_4$ HMSs.

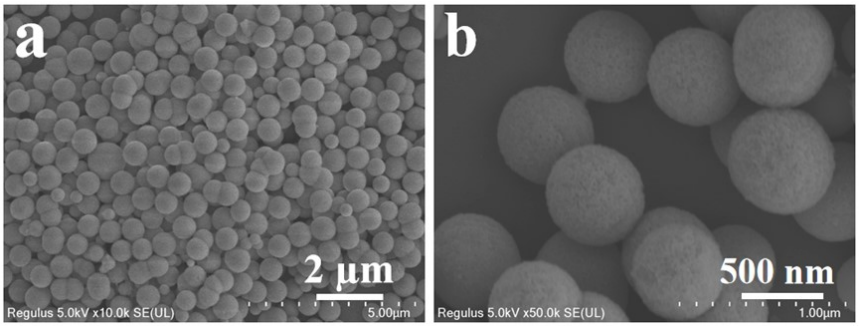

Figure S4. (a, b) SEM images of Bi_2O_3 precursor.

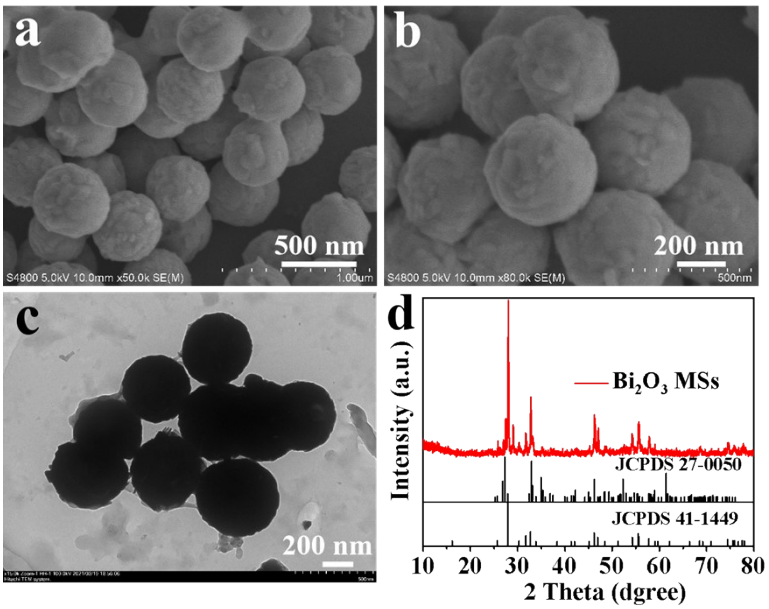

Figure S5. (a, b) SEM images, (c) TEM image and (d) XRD pattern of Bi_2O_3 MSs.

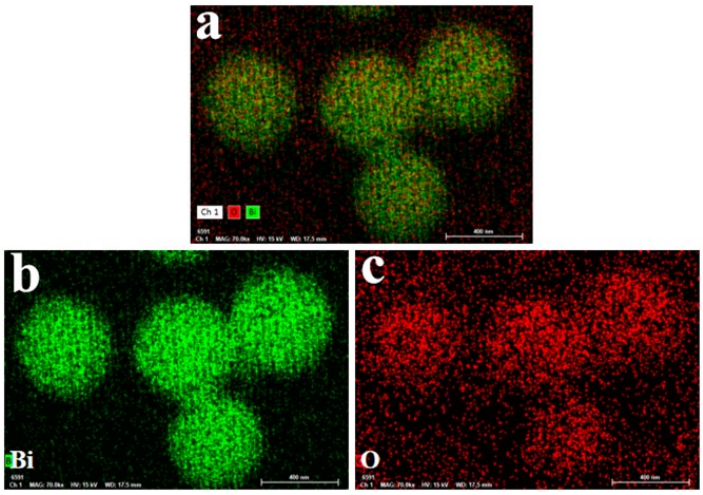

Figure S6. The SEM mapping images of Bi_2O_3 MSs.

The low/high magnification SEM images of the precursor NiCo-LDH/C are exhibited in Fig S1. It is clearly seen that the product has a spherical morphology with nanosheets. The diameter size of NiCo-LDH/C is around 900 nm. After annealing, the surface of $NiCo_2O_4$ HMSs become a little rough, and the size of the product becomes a little smaller than NiCo-LDH/C (Fig S2a, b). As shown in TEM image (Fig S2c), it is obvious observed that the product has a porous hollow spherical structure. Several featured peaks assigned to $NiCo_2O_4$ (JPCDS no. 20-0781) can be revealed in the XRD pattern (Fig S2d). The SEM elemental mapping confirms that the Ni, Co and O are uniform distributed in the $NiCo_2O_4$ HMSs (Fig S3).

Fig S4 shows low/high magnification SEM images of the solid spherical Bi_2O_3/C precursor, with the diameter size of 650 nm. The SEM, TEM and XRD pattern of the obtained calcined yellow product Bi_2O_3 are shown in Fig S5. As can be seen from the SEM images (Fig S5a, b)，the solid sphere size of Bi_2O_3 decreases slightly, which is verified by the TEM image as manifested in Fig S5c. The crystalline and phase purity of the prepared Bi_2O_3 microspheres were detected by the XRD (Fig S5d). It is obvious that the remarkable peaks correspond to the standard card of Bi_2O_3 (JCPDS no. 27-0050/41-1449). The SEM elemental mapping images (Fig S6) for Bi_2O_3 MSs confirm homogeneous distribution and presence of Bi and O elements, respectively.

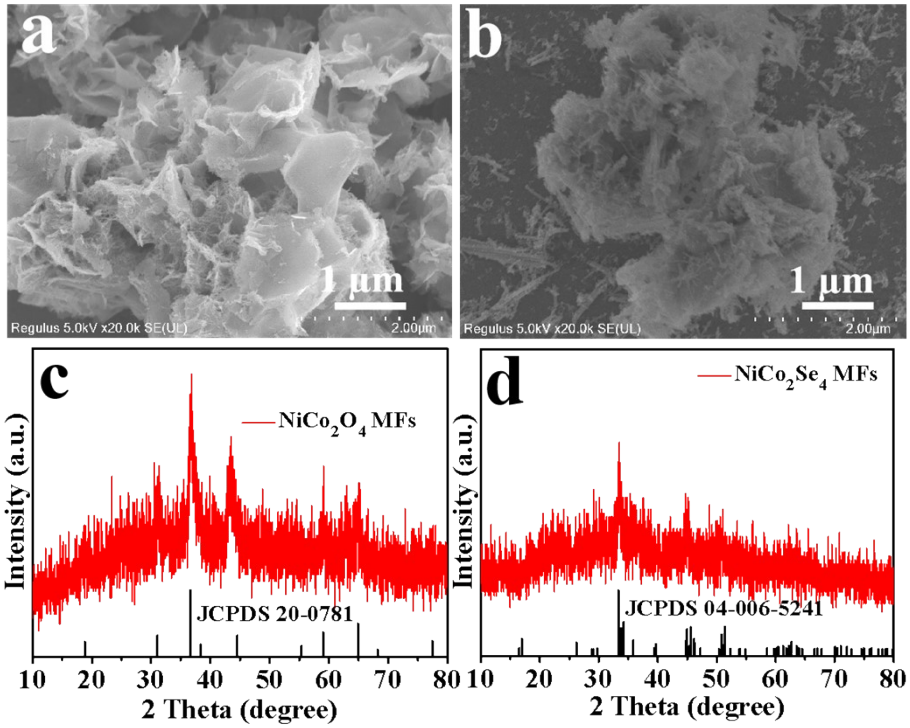

Figure S7. The SEM images of $NiCo_2O_4$ MFs (a) and $NiCo_2Se_4$ MFs (b). The XRD patterns of $NiCo_2O_4$ MFs (c) and $NiCo_2Se_4$ MFs (d).

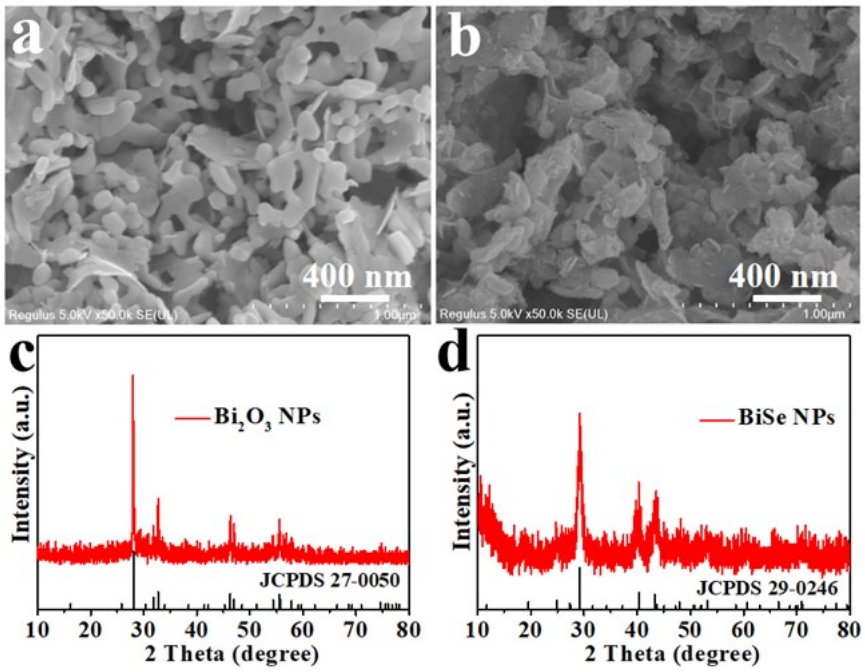

Figure S8. The SEM images of Bi_2O_3 NPs (a) and BiSe NPs (b). The XRD patterns of Bi_2O_3 NPs (c) and BiSe NPs (d).

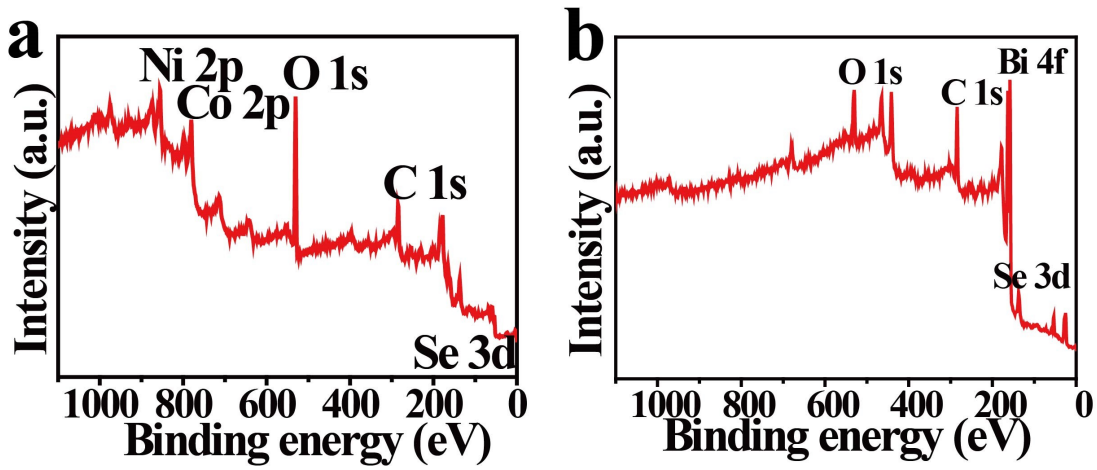

Figure S9. XPS survey spectrum of $NiCo_2Se_4$ HMSs (a) and BiSe HMS (b).

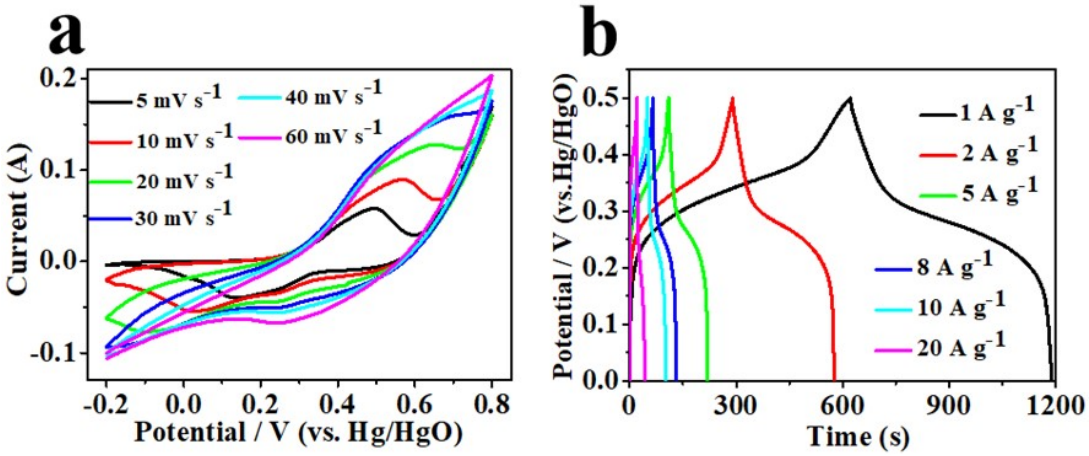

Figure S10. The CV curves at various scan rates and GCD curves at different current densities of the $NiCo_2Se_4$ MFs electrode.

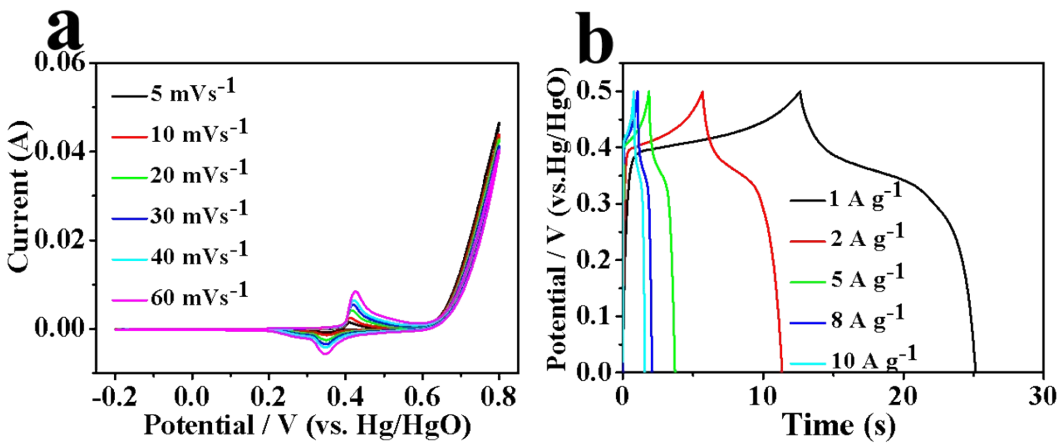

Figure S11. The CV curves at different scan rats (a) and the GCD curves at various current density (b) of the nickel foam electrode.

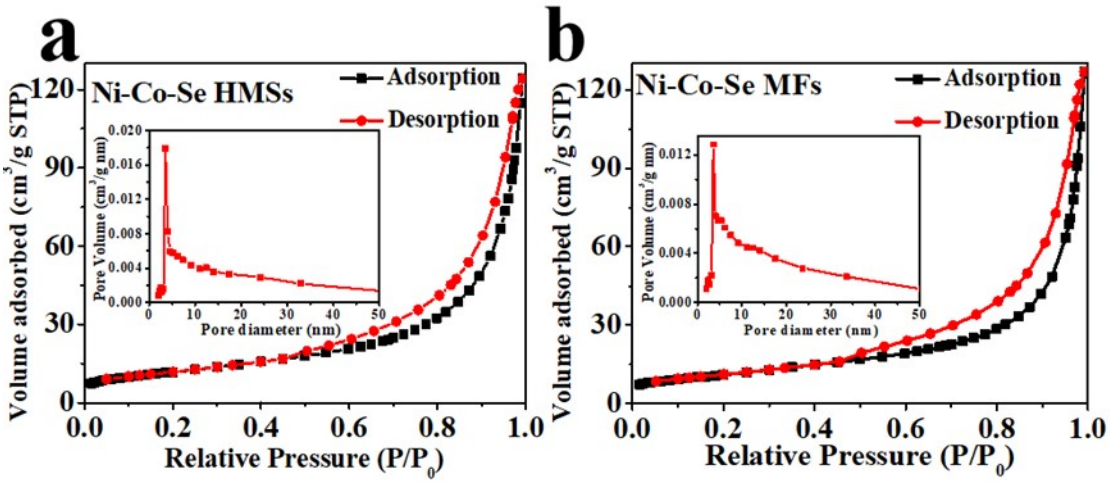

Figure S12. Nitrogen adsorption/desorption isotherm and pore size distribution curve (inset) of $NiCo_2Se_4$ HMSs (a) and $NiCo_2Se_4$ MFs (b).

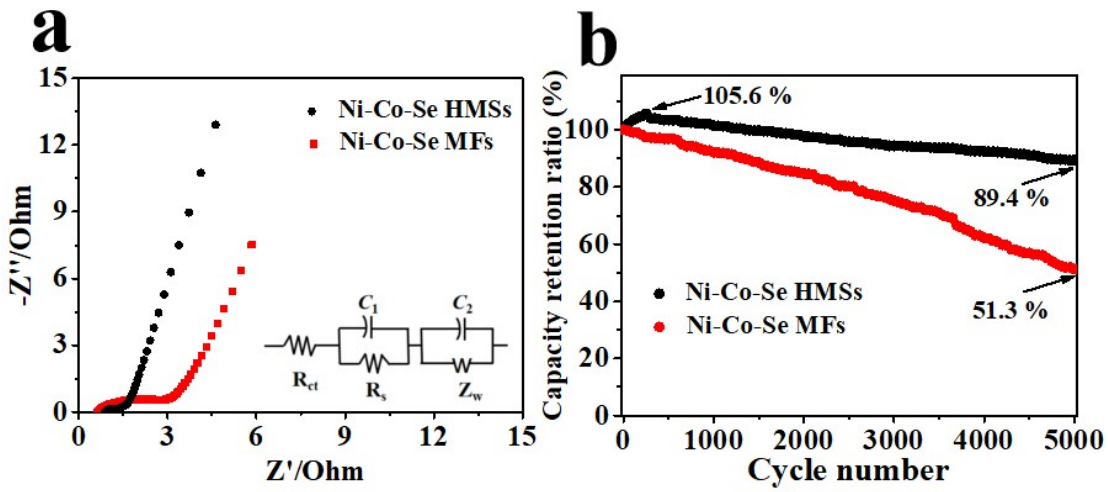

Figure S13. (a) The Nyquist plots of $NiCo_2Se_4$ HMSs and $NiCo_2Se_4$ MFs electrodes, and the inset is the equivalent circuit diagram, (b) the comparison of cycle performance for $NiCo_2Se_4$ HMSs and $NiCo_2Se_4$ MFs electrodes.

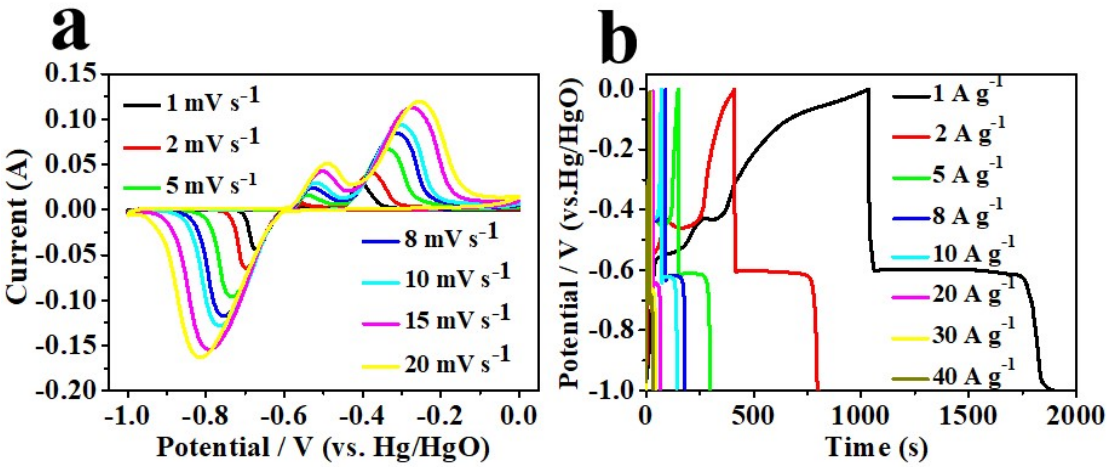

Figure S14. The CV curves at various scan rates and GCD curves at different current densities of the BiSe NPs electrode.

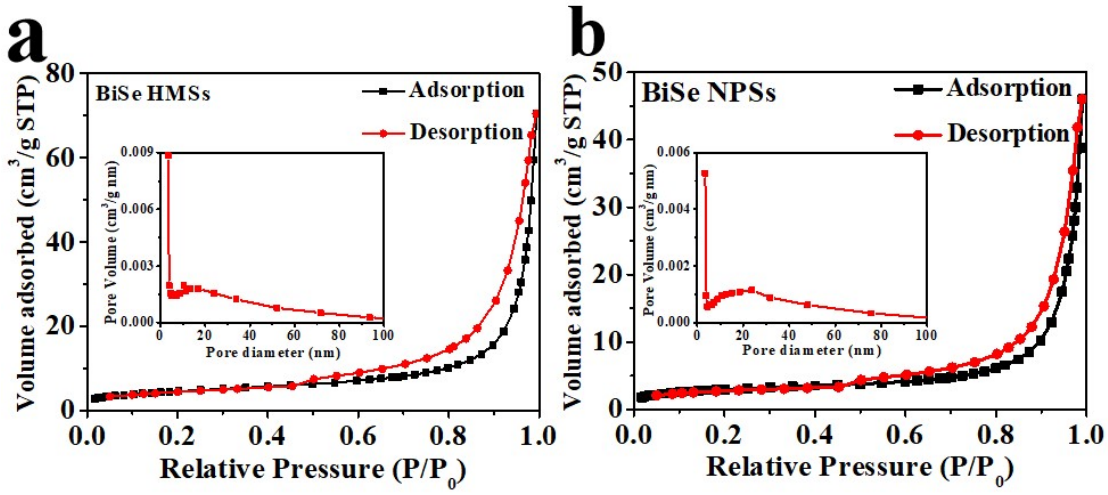

Figure S15. Nitrogen adsorption/desorption isotherm and pore size distribution curve (inset) of BiSe HMSs (a) and BiSe NPs (b).

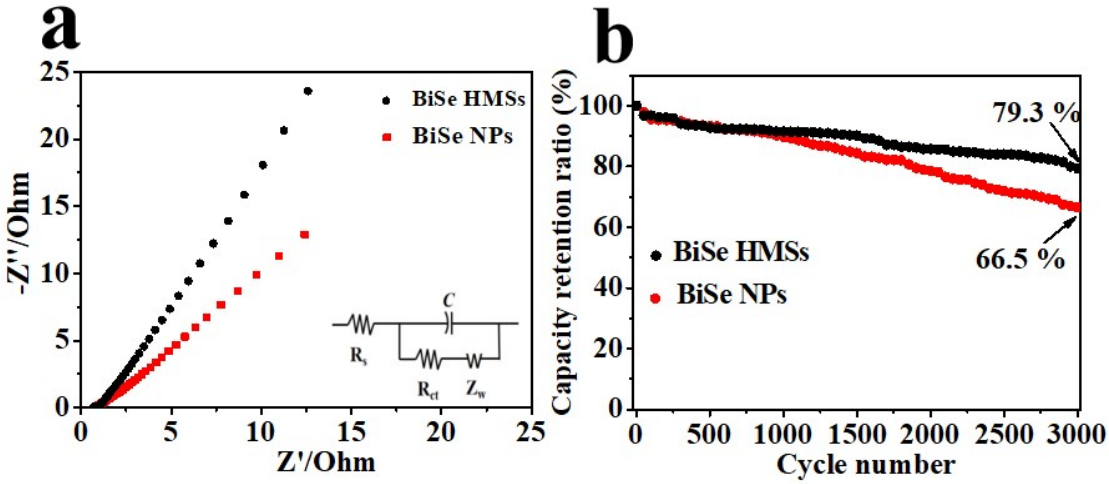

Figure S16. (a) The Nyquist plots of BiSe HMSs and BiSe MFs electrodes, the inset is the equivalent circuit diagram, (b) the comparison of cycle performance for BiSe HMSs and BiSe NPs electrodes.

The electrochemical performances of $NiCo_2O_4$ HMSs and $NiCo_2O_4$ MFs electrodes.

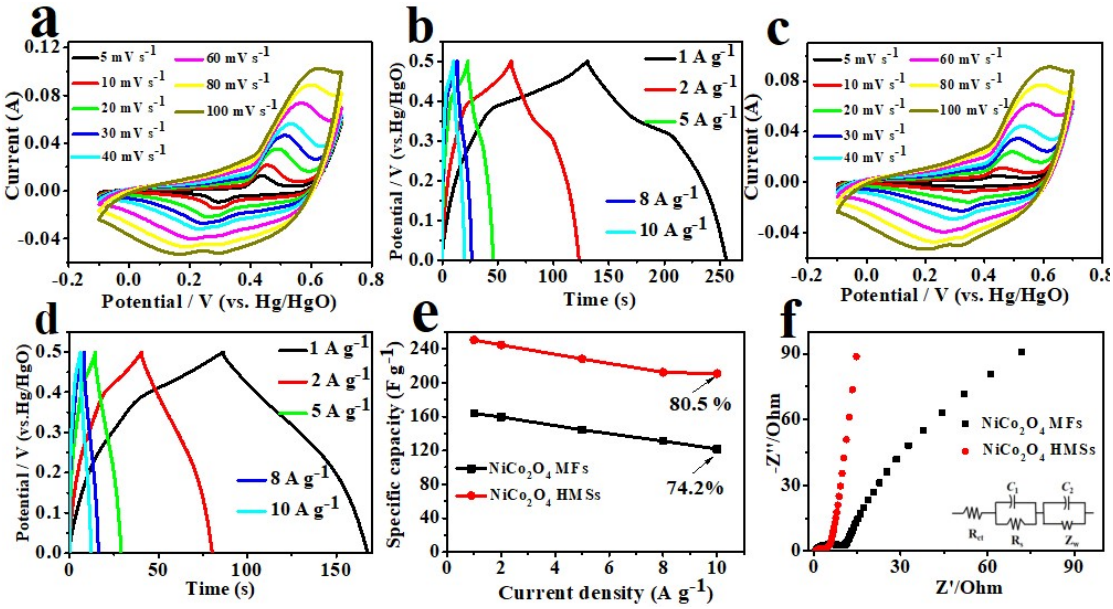

Figure S17. (a, c) the CV curves at various scan rates, (b, d) the GCD curves at different current densities, (e) the rate performance and the Nyquist plots of $NiCo_2O_4$ HMSs (a, b) and $NiCo_2O_4$ MFs (c, d) electrodes.

Fig. S17a, c displays the CV curves of $NiCo_2O_4$ HMSs and $NiCo_2O_4$ MFs electrodes at different scan rates with the potential window of -0.1-0.7 V. And a pair of redox peaks indicate the pseudocapacitance behavior of $NiCo_2O_4$ in 3 M KOH electrolyte. The GCD curves of $NiCo_2O_4$ HMSs and $NiCo_2O_4$ MFs electrodes are shown in Fig. S 17b, d. The specific capacitances of $NiCo_2O_4$ HMSs electrode are calculated to 250.4, 244.5, 228, 212.3 and 210.6 F g^{-1} at various current densities of 1-10 A g^{-1}, respectively. And $NiCo_2O_4$ MFs electrode delivers the capacitances of 163.8, 159.5, 144.3, 131 and 121.6 F g^{-1}. As shown in Fig. S17e, $NiCo_2O_4$ HMSs exhibits higher rate capability of 80.5 % than $NiCo_2O_4$ MFs electrode (74.2 %). As shown in Fig. S17f, the fitting results proves that

$NiCo_2O_4$ HMSs electrode (R_{ct} = 3.80 Ω, R_s = 0.68 Ω) has a higher electrical conductivity and faster electron transport compared to $NiCo_2O_4$ MFs electrode (R_{ct} = 8.03 Ω, R_s = 0.74 Ω).

The electrochemical performances of Bi_2O_3 MSs and Bi_2O_3 NPs electrodes.

The CV curves exhibit a pair of redox peaks in Fig. S18a,c correspond to the following reactions for Bi_2O_3[1]: $Bi_2O_3 + 3H_2O + 6e^- \leftrightarrow 2Bi + 6OH^-$, implying the typical pseudocapacitive behaviors [2]. A small peak at about -0.5 V, which may be ascribe to the catalytic induction or oxidation of Bi according to other literatures[3, 4]. Fig. S18b, d show the GCD curves of Bi_2O_3 MSs and Bi_2O_3 NPs electrodes at different current densities in 3 M KOH electrolyte. The specific capacitances of Bi_2O_3 MSs electrode with increasing current densities of 1-20 A g^{-1} are 914, 882.4, 807, 792, 788 and 80 F g^{-1}, respectively. Compared to Bi_2O_3 MSs, the specific capacitances of Bi_2O_3 NPs electrode are 613.5, 575.5, 531, 529.2, 521.4 and 45.2 F g^{-1}, respectively. Bi_2O_3 MSs electrode exhibits higher specific capacitance (914 F g^{-1} at 1 A g^{-1}) than Bi_2O_3 NPs electrode (613.4 F g^{-1} at 1 A g^{-1}). As shown in Fig. S18e, when increasing current densities from 1 to 10 A g^{-1}, Bi_2O_3 MSs and Bi_2O_3 NPs electrodes both deliver better rate capabilities (86.2 % and 85 %), while the capacitances decrease at 20 A g^{-1} rapidly, due to the lack of time for

redox reactions. Similarly, the EIS technique is also employed to understand that Bi_2O_3 MSs electrode has better electrochemical performance than Bi_2O_3 NPs electrode. A large slope of line at low-frequency region, a small semicircle (R_{ct} = 0.07 Ω) and short x-intercept (R_s = 0.79 Ω) at high-frequency region, demonstrating Bi_2O_3 MSs electrode has a higher electric conductivity and fast ion diffusion/ charge transport, compared with the fitting results (R_{ct} = 7.21 Ω, R_s = 1.02 Ω) for Bi_2O_3 NPs electrode (Fig. S18f).

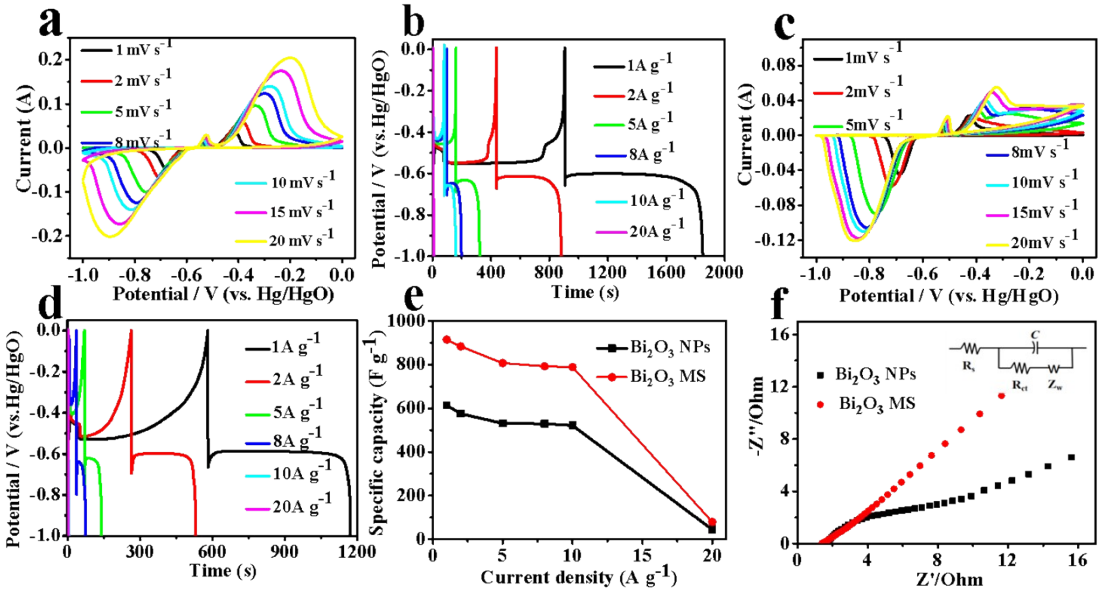

Figure S18. (a, c) the CV curves at various scan rates, (b, d) the GCD curves at different current densities, (e) the rate performance and the Nyquist plots of the Bi_2O_3 MSs (a, b) and Bi_2O_3 NPs (c, d) electrodes.

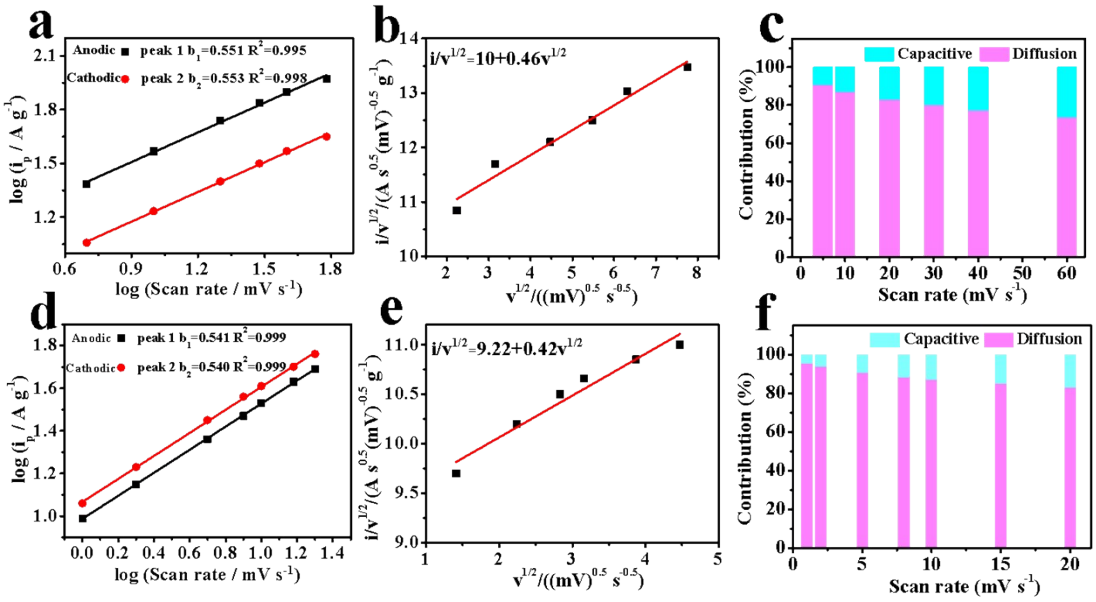

Figure S19. (a, d) determination of b value using the relationship between log (peak current) and log (scan rate), (b, e) $i/v^{1/2}$ vs. $v^{1/2}$ plot using the anodic peak 1 current, (c, f) the capacitive and diffusion-controlled contributions of the Ni-Co-Se/BiSe HMSs electrode and the total capacitance contributions, respectively.

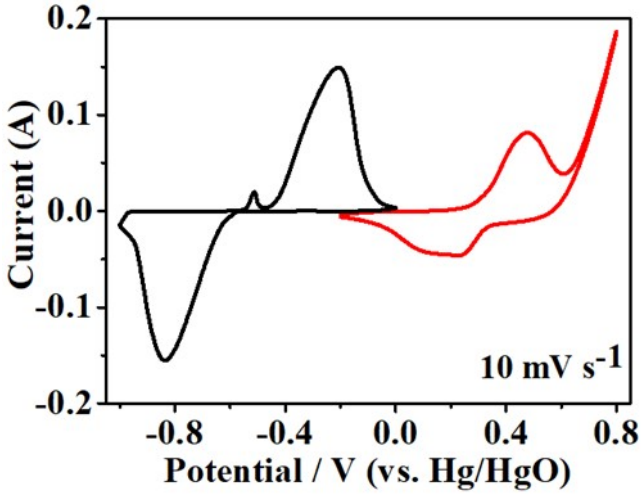

Figure S20. CV curves of the BiSe HMSs and Ni-Co-Se HMSs electrodes obtained at 10 mV s^{-1} in a three-electrode system.

Table S1. The electrochemical performance comparison of $NiCo_2Se_4$ HMSs electrode with the other previously reported

Electrode materials	Electrolyte	C_{sp} (F g^{-1}) /C.D (A g^{-1})	CR(%)/CN	Ref.
$NiCo_2Se_4$ HMSs	3 M KOH	1874.6/1	89.4/5000	This work
$CoNi_2Se_4$ nanoparticles	6 M KOH	1585/1	83.31/3000	[5]
$NiSe_2/CoSe_2$	3 M KOH	1668/1	84.7/5000	[6]
$CoSe_2$ nanosheets	6 M KOH	333/1	100.97/25000	[7]
NiSe nanoparticles on G	6 M KOH	1280/1	98/2500	[8]
$NiCo_2Se_4$/RGO	6 M KOH	1776/2	86/3000	[9]
NiSe-$Ni_{0.85}Se$	2 M KOH	1487/1	80/5000	[10]

C_{sp}: Specific capacitance, C.D Current density, CR: Capacitance retention, CN: cycling number, G: graphene nanosheets, RGO: reduced graphene oxide.

Table S2. The electrochemical performance comparison of BiSe HMSs electrode with the other previously reported

Electrode materials	Electrolyte	C_{sp} (F g^{-1}) /C.D (A g^{-1})	CR(%)/CN	Ref.
BiSe HMSs	3 M KOH	1293/1	78/3000	This work
Bi_2Se_3-MnO_2 nanotube	0.5 M Na_2SO_4	438/1	86/2000	[11]
Bi_2O_3@C microrods	1 M KOH	1378/1	93/4000	[12]
GF@$BiFeO_3$-NC	6 M KOH	456/1	71.4/6000	[13]
$Bi_{18}SeO_{29}$/BiSe	2 M KOH	471.3/0.5	68/5000	[14]
FeO_x nanoparticle	6 M KOH	436/1	89/5000	[15]
graphene-Mn_3O_4	1 M H_2SO_4	660/0.2	89/4000	[16]

GF: graphite fibers, NC: N-doped carbon.

References

[1] G. Zan, T. Wu, P. Hu, Y. Zhou, S. Zhao, S. Xu, J. Chen, Y. Cui, Q. Wu, An approaching-theoretical-capacity anode material for aqueous battery: Hollow hexagonal prism Bi_2O_3 assembled by nanoparticles, Energy Stor. Mater. 28 (2020) 82-90.

[2] O. Üner, N. Aslan, A. Sarıoğlu, F. Semerci, M.M. Koç, Facile preparation of commercial Bi_2O_3 nanoparticle decorated activated carbon for pseudocapacitive supercapacitor applications, J. Mater. Sci.: Mater. Electron. 32 (2021) 15981-15994.

[3] S.X. Wang, C.C. Jin, W.J. Qian, Bi_2O_3 with activated carbon composite as a supercapacitor electrode, J. Alloys Compd. 615 (2014) 12-17.

[4] Y. Qiu, H. Fan, X. Chang, H. Dang, Q. Luo, Z. Cheng, Novel ultrathin Bi_2O_3 nanowires for supercapacitor electrode materials with high performance, Appl. Surf. Sci. 434 (2018) 16-20.

[5] J.A. Rajesh, Y.-H. Lee, Y.-H. Yun, V.H.V. Quy, S.-H. Kang, H. Kim, K.-S. Ahn, Potentiostatic deposition of $CoNi_2Se_4$ nanostructures on nickel foam as efficient battery-type electrodes for supercapacitors, J. Electroanal Chem. 850 (2019) 113371.

[6] G. Qu, X. Zhang, G. Xiang, Y. Wei, J. Yin, Z. Wang, X. Zhang, X. Xu, ZIF-67 derived hollow Ni-Co-Se nano-polyhedrons for flexible hybrid supercapacitors with remarkable electrochemical performances, Chin. Chem. Lett. 31 (2020) 2007-2012.

[7] S. Liu, S. Sarwar, J. Wang, H. Zhang, T. Li, J. Luo, X. Zhang, The microwave synthesis of porous $CoSe_2$ nanosheets for super cycling performance supercapacitors, J. Mater. Chem. C 9 (2021) 228-237.

[8] B. Kirubasankar, V. Murugadoss, J. Lin, T. Ding, M. Dong, H. Liu, J. Zhang, T. Li, N. Wang, Z. Guo, S. Angaiah, In situ grown nickel selenide on graphene nanohybrid electrodes for high energy density asymmetric supercapacitors, Nanoscale 10 (2018) 20414-20425.

[9] S. Ghosh, P. Samanta, N.C. Murmu, T. Kuila, Investigation of electrochemical charge storage in nickel-cobalt-selenide/reduced graphene oxide composite electrode and its hybrid supercapacitor device, J. Alloys Compd. 835 (2020) 155432.

[10] Y. Bai, W. Shen, K. Song, S. Zhang, Y. Wang, T. Xu, J. Xu, S. Dai, X. Wang, Controlled synthesis of NiSe-$Ni_{0.85}Se$ nanocomposites for high-performance hybrid supercapacitors, J. Electroanal Chem. 880 (2021) 114795.

[11] M. Pradhan, R. Chakraborty, S. Rudra, S. Koley, P.K. Maji, A.K. Nayak, S. Das, U. Nandi, Intercalation pseudocapacitance in Bi_2Se_3-MnO_2 nanotube composite for high electrochemical energy storage, Electrochim. Acta 367 (2021) 137531.

[12] X. Yu, J. Sun, W. Zhao, S. Zhao, H. Chen, K. Tao, Y. Hu, L. Han, MOF-derived Bi_2O_3@C microrods as negative electrodes for advanced asymmetric supercapacitors, RSC Adv. 10 (2020) 14107-14112.

[13] Q. Pan, C. Yang, Q. Jia, W. Qi, H. Wei, M. Wang, S. Yang, B. Cao, Oxygen-deficient $BiFeO_3$-NC nanoflake anodes for flexible battery-supercapacitor hybrid devices with high voltage and long-term stability, Chem. Eng. J. 397 (2020) 125524.

[14] G. Ma, F. Hua, K. Sun, E. Fenga, H. Peng, Z. Zhang, Z. Lei, Nanostructure selenium compounds as pseudocapacitive electrodes for high-performance asymmetric supercapacitor, R. Soc. Open Sci. 5 (2018) 171186.

[15] E. Samuel, B. Joshi, H.S. Jo, Y.I. Kim, S. An, M.T. Swihart, J.M. Yun, K.H. Kim, S.S. Yoon, Carbon nanofibers decorated with FeO nanoparticles as a flexible electrode material for symmetric supercapacitors, Chem. Eng. J. 328 (2017) 776-784.

[16] R. Boddula, R. Bolagam, P. Srinivasan, Incorporation of graphene-Mn_3O_4 core into polyaniline shell: supercapacitor electrode material, Ionics 24 (2017) 1467-1474.